Supplementary Information

Polarization-Sensitive In-Sensor Computing in Chiral Organic Integrated 2D p-n Heterostructures for Mixed-Multimodal Image Processing

Je-Jun Lee[1,†], Seong-Jun Han[1,2,†], Changsoon Choi[1], Chaewon Seo[3], Seungkwon Hwang[4], Jihyun Kim[5], Jung Pyo Hong[1,2], Jisu Jang[1], Jihoon Kyhm[6], Jung Woo Kim[1,2], Byoung-Soo Yu[1,7], Jung Ah Lim[7,8] Gunuk Wang[2], Joohoon Kang[5], Yonghun Kim[4], Suk-kyun Ahn[3,*], Jongtae Ahn[9,*], and Do Kyung Hwang[1,2,7,*]

[1]Center of Quantum Technology, Post-Silicon Semiconductor Institute, Korea Institute of Science and Technology (KIST), Seoul 02792, Republic of Korea

[2]KU-KIST Graduate School of Converging Science and Technology, Korea University, Seoul, Republic of Korea

[3]School of Chemical Engineering, Pusan National University, Busan 46241, Republic of Korea

[4]Energy and Environment Materials Research Division, Korea Institute of materials Science (KIMS), Changwon, Korea

[5]Department of Chemical and Biomolecular Engineering, Yonsei University, Seoul 03722, Republic of Korea

[6]Technology Support Center, Research Resources Division, Korea Institute of Science and Technology (KIST), Seoul 02792, Republic of Korea

[7]Division of Nanoscience & Technology, KIST School, University of Science and Technology (UST), Seoul, Republic of Korea

[8]Soft Hybrid Materials Research Center, Advanced Materials Research Division, Korea Institute of Science and Technology (KIST), Seoul 02792, Republic of Korea

[9]Department of Physics, Changwon National University, Changwon 51139, Republic of Korea

[†]These authors contributed equally to this work

*E-mail: skahn@pusan.ac.kr, jongtae@changwon.ac.kr, dkhwang@kist.re.kr

Contents

Supplementary Figures

1. Optical microscopy image of CIPs.
2. Circular dichroism measurements of CLCN films.
3. CLCN films thickness-dependent characteristics.
4. Transmission spectra of CLCN films depending on concentrations of chiral dopants.
5. Thickness measurements and crystallinity verification of the van der Waals (vdW) p-n diode via atomic force microscopy and Raman spectroscopy.
6. Spectral responsivity measurements for 520 nm- and 830 nm-targeted R-form CIPs.
7. Geometrical dependence of short-circuit current (I_{SC}) in R-form CIPs.
8. Dissymmetry factors of CIPs.
9. Measured noise power spectral density for the CLCN-integrated photodiodes.
10. Cycle-to-cycle variations of L-form CIPs illuminated by RH-CPL.
11. Frequency responses of CLCN-integrated photodiodes.
12. Simulated result for separated mixed-MNIST pattern.
13. Simulated result for separated mixed-fashion-MNIST pattern.
14. Recognition result and following confusion matrix for mixed-fashion-MNIST pattern.
15. Comparison of various in-sensor computing technologies.
16. Polarization modulation process by half-wave and quarter-wave retarders.
17. Optical microscopy image of zero-dimensional (1×1) polarimetric array of CIPs.

18. Photo of 1×3 polarimetric kernel array for mixed identity function and Sobel-x function.

19. Fabrication process of localized CIPs.

20. Transmittance of localized CLCN.

21. *I*–*V* characteristics of localized CIPs.

22. Applications of mixed-kernel image processing for blurring and sharpening.

23. Conceptual design of a 3×3 polarimetric kernel array.

Supplementary Table

1. Comparison of recent in-sensor computing technologies.

2. Benchmarking table of optoelectronic properties of circularly polarized light detectors.

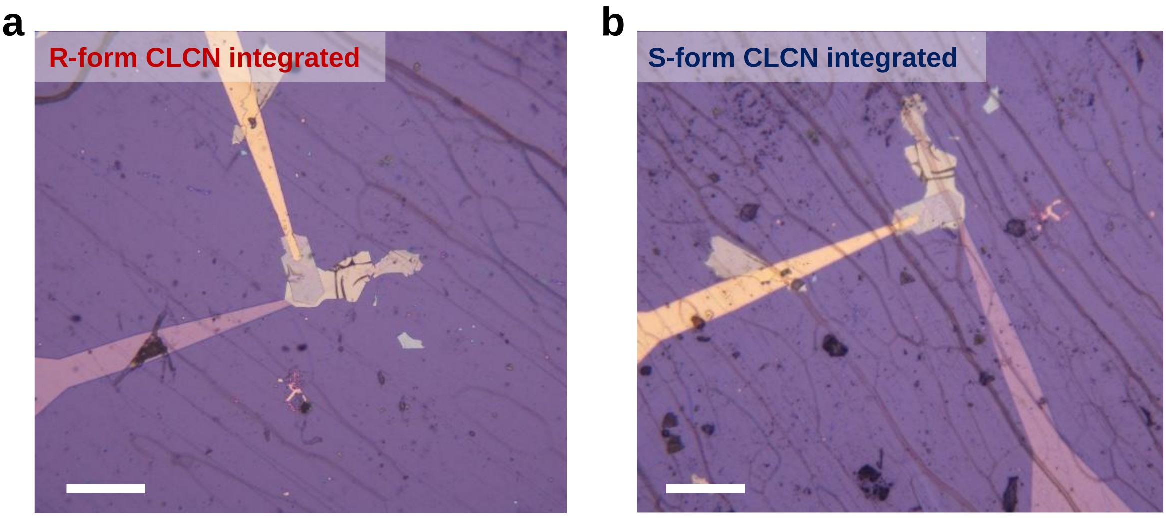

Supplementary Figure 1. Optical microscopy image of an **a,** R-form and **b,** S-form CIPs. Scale bar is 100 μm.

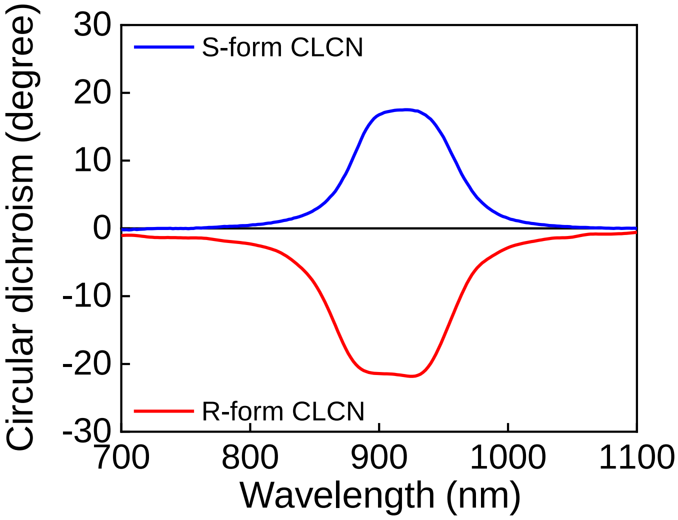

Supplementary Figure 2. Circular dichroism measurements of CLCN films.

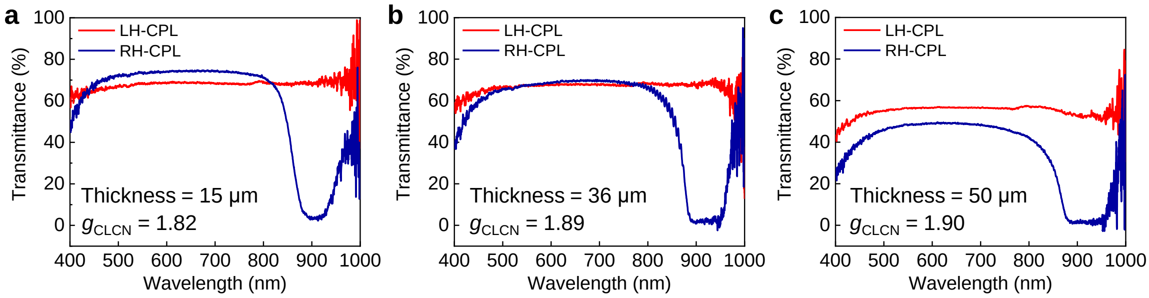

Supplementary Figure 3. Transmittance of R-form CLCN films with a thickness of **a,** 15 μm, **b,** 36 μm, and **c,** 50 μm.

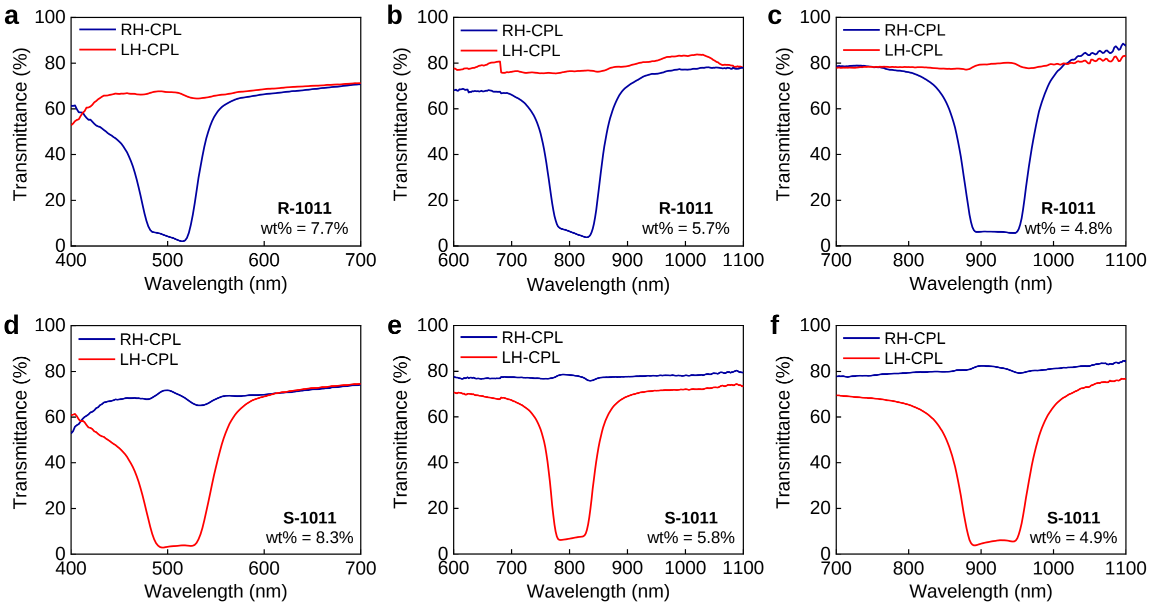

Supplementary Figure 4. Transmission spectra of CLCN films depending on concentrations of chiral dopants.

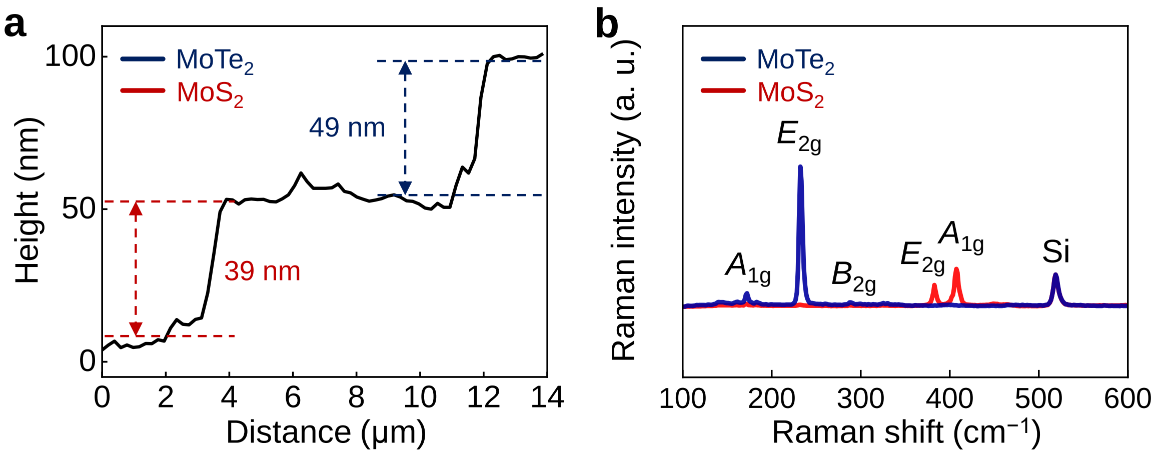

Supplementary Figure 5. Verification of **a,** thickness and **b,** crystallinity of the vdW p-n diode using atomic force microscopy and a Raman spectrometer, respectively. Detection of the A_{1g} / E_{2g} Raman peaks of $MoTe_2$ and MoS_2 was confirmed as 171.4 / 231.3 cm^{-1} and 407.1 / 382.1 cm^{-1}, respectively, under incident beam conditions of 532 nm and 5 mW.

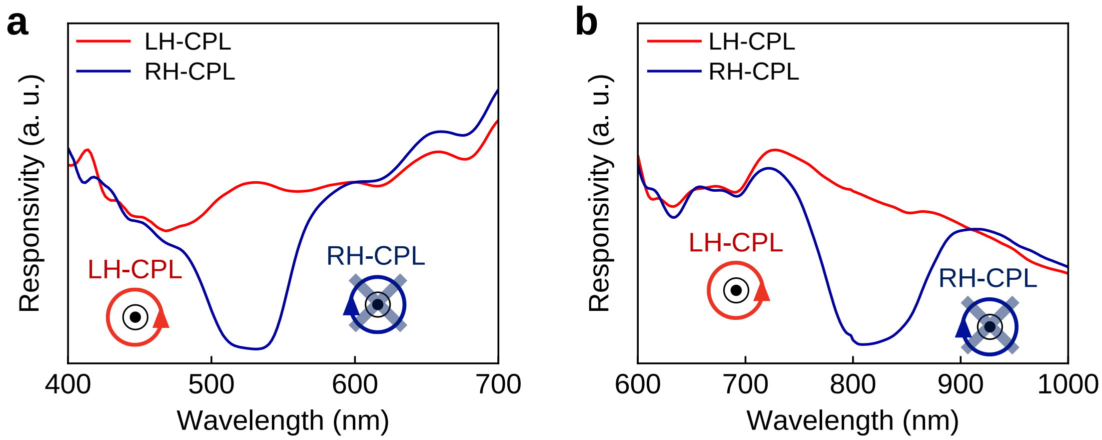

Supplementary Figure 6. Spectral responsivity of **a,** 520 nm- and, **b,** 830 nm-targeted R-form CIPs.

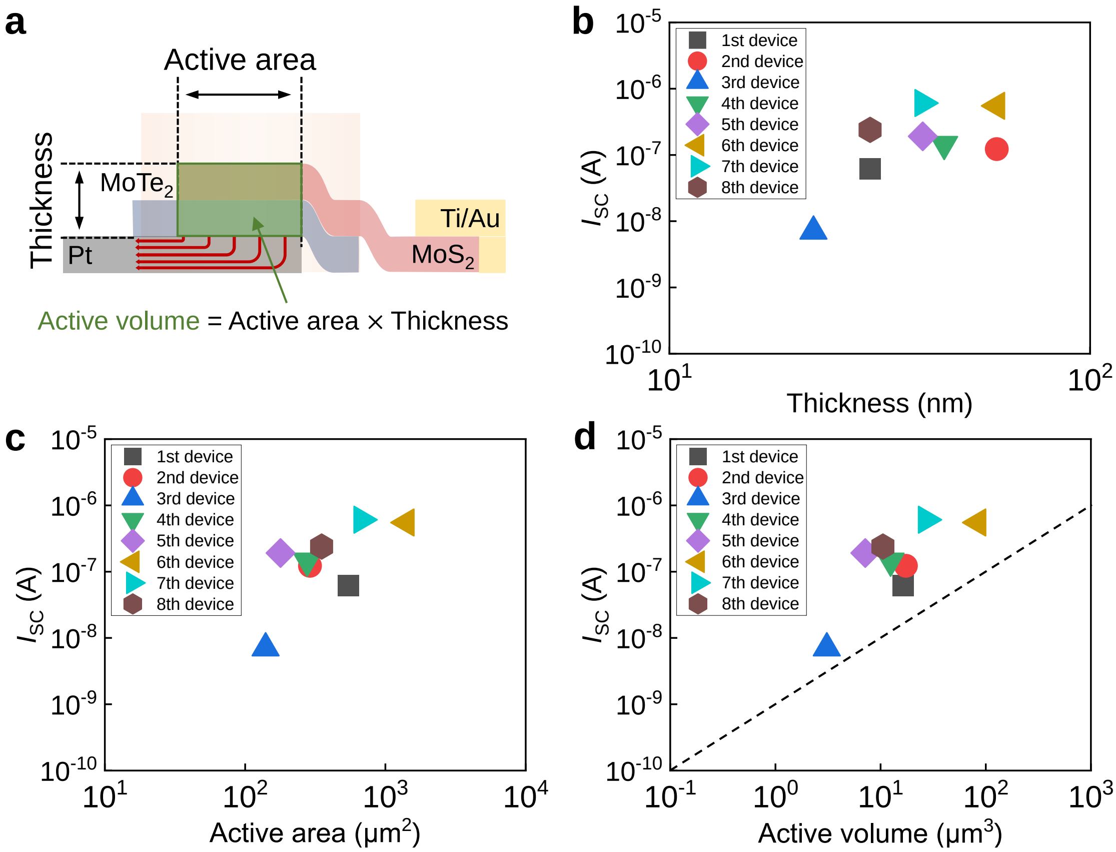

Supplementary Figure 7. Geometrical dependence of short-circuit current (I_{SC}) in R-form CIPs. **a,** Schematic of the photodiode geometry, indicating the regions defined as the active area, thickness, and active volume. Short-circuit current (I_{SC}) dependence on **b,** total thickness, **c,** active area, **d,** active volume. Data were obtained under left-handed circularly polarized light (LH-CPL) using a light source (904 nm and 100 mW cm^{-2}) for eight R-form CIPs.

Our statistical analysis confirms that p–n junctions with a larger active area and total thickness (i.e., the combined thickness of the p- and n-type layers) generally exhibit higher short-circuit current (I_{SC}) (Supplementary Figs. 7a-c). Moreover, a near-linear trend is observed between I_{SC} and the active volume, defined as the product of the thickness and the active region (Pt/MoS_2/$MoTe_2$). This trend holds when the photoresponse from the remaining area of the vdW heterojunction (MoS_2/$MoTe_2$), from the each individual material, and variations in the thickness ratio between MoS_2 and $MoTe_2$ are not considered (Supplementary Fig. 7d).

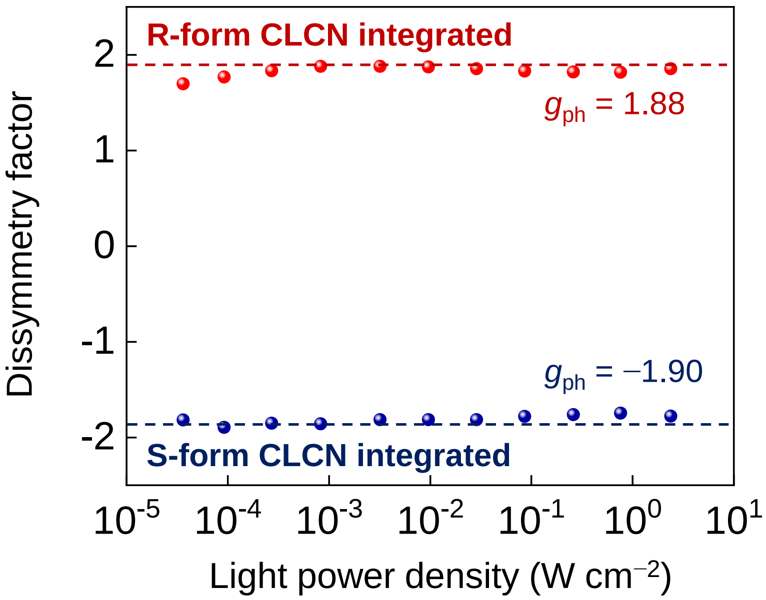

Supplementary Figure 8. Dissymmetry factors of CIPs extracted from the data Figure 2e and 2f.

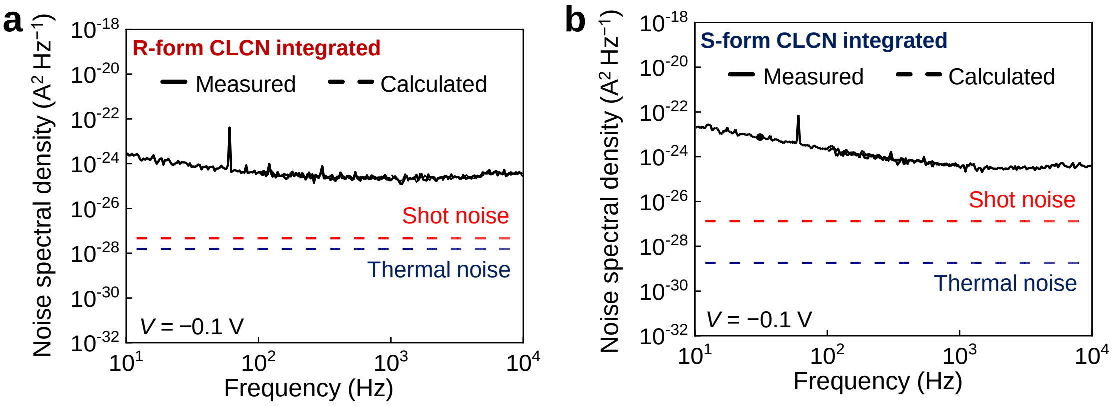

Supplementary Figure 9. Noise power spectral density characteristics of **a,** R-form CIP and **b,** S-form CIP.

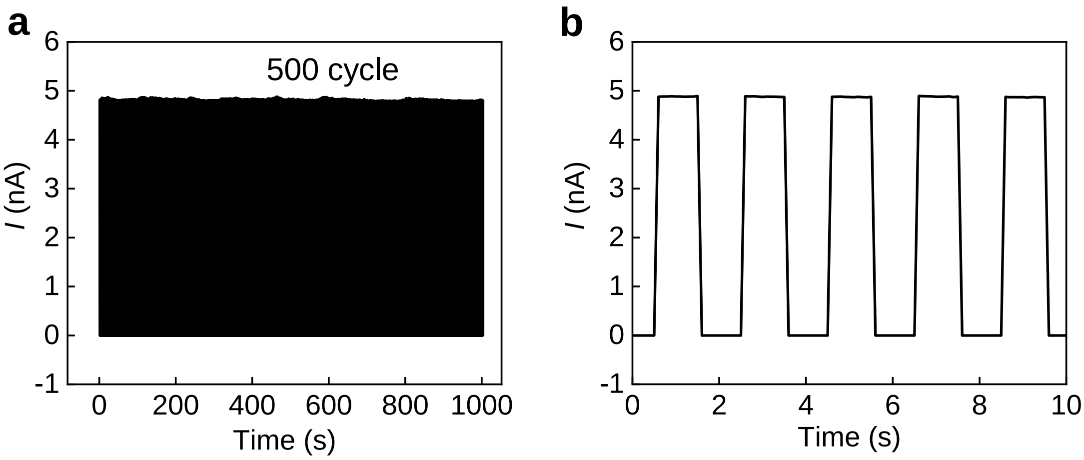

Supplementary Figure 10. Cycle-to-cycle variations of L-form CIPs illuminated by RH-CPL using a light source (904 nm and 10 mW cm^{-2}).

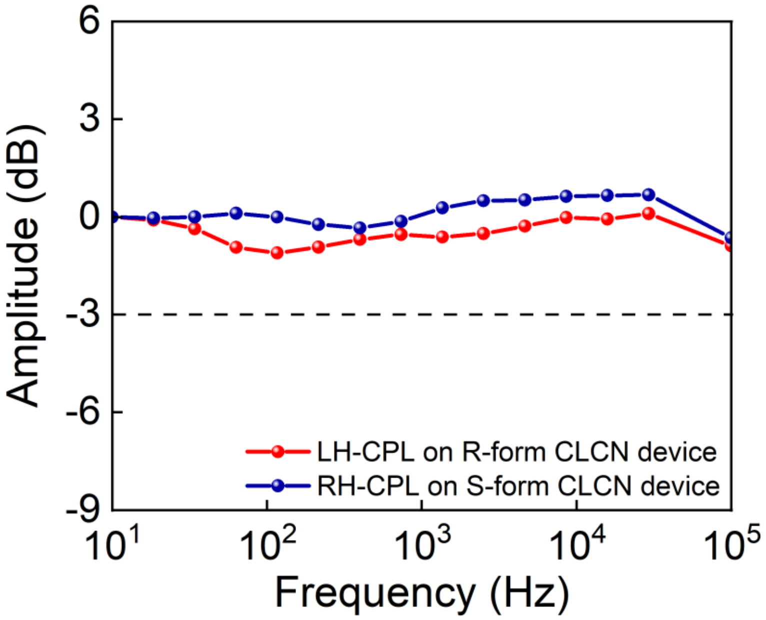

Supplementary Figure 11. Frequency response analysis in both R-form and S-form configurations under $V = 0$ V.

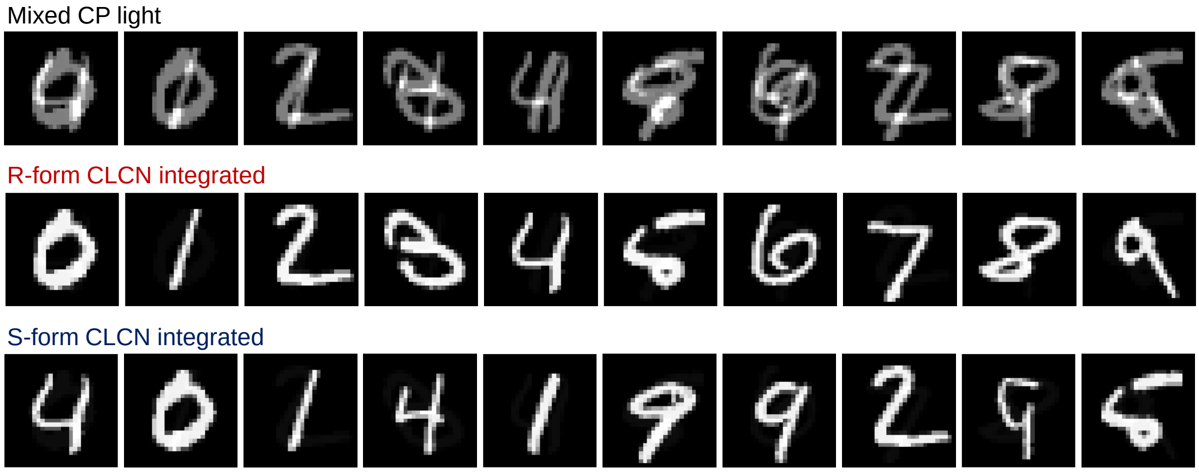

Supplementary Figure 12. Simulated result for separated mixed-MNIST pattern.

Supplementary Figure 13. Simulated result for separated mixed-fashion-MNIST pattern[S1] (© 2017 Zalando SE), used under the MIT License.

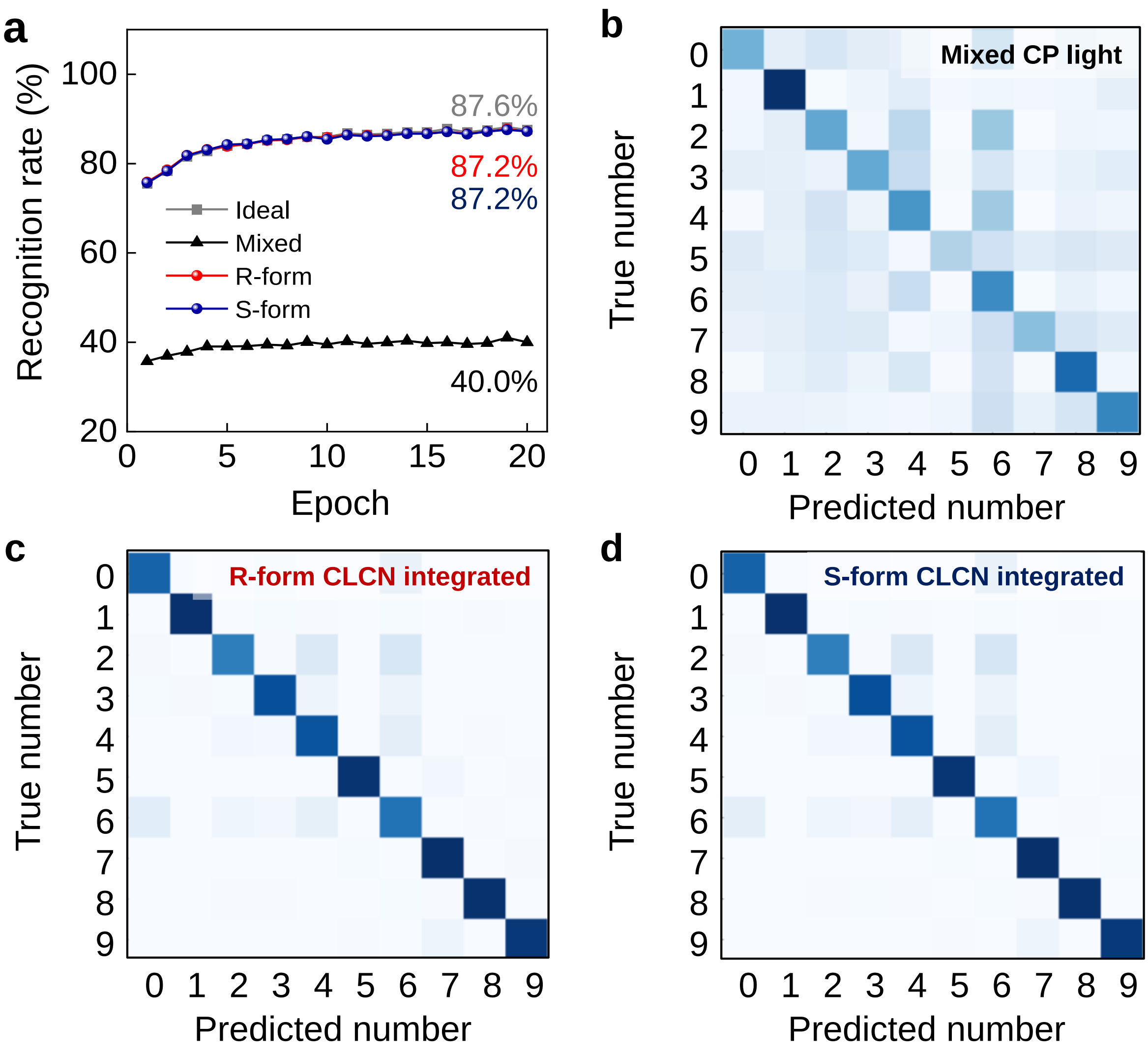

Supplementary Figure 14. Recognition result and following confusion matrix for mixed-fashion-MNIST pattern. In the Fashion MNIST dataset, the numbers 0-9 correspond to the following clothing items: 0 - T-shirt/top, 1 - Trouser, 2 - Pullover, 3 - Dress, 4 - Coat, 5 - Sandal, 6 - Shirt, 7 - Sneaker, 8 - Bag, and 9 - Ankle boot.

	Conventional in-sensor computing	Non-reconfigurable in-sensor computing	In-sensor dynamic computing	Mixed-multimodal computing
Circuit configuration	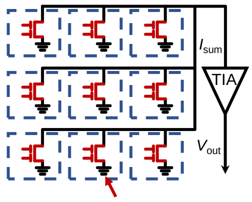 Reconfigurable devices	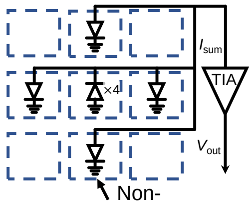 Non-reconfigurable devices	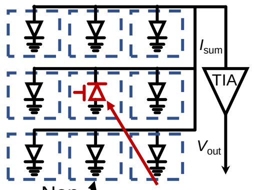 Non-reconfigurable devices; Reconfigurable devices	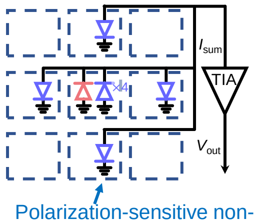 Polarization-sensitive non-reconfigurable devices
Circuit Complexity	High	low	Moderate	Low
Universality in a single circuit	High	low	low	Moderate
Kernel optimization	Possible	Impossible	Possible	Possible

Supplementary Figure 15. Comparison of various in-sensor computing technologies.

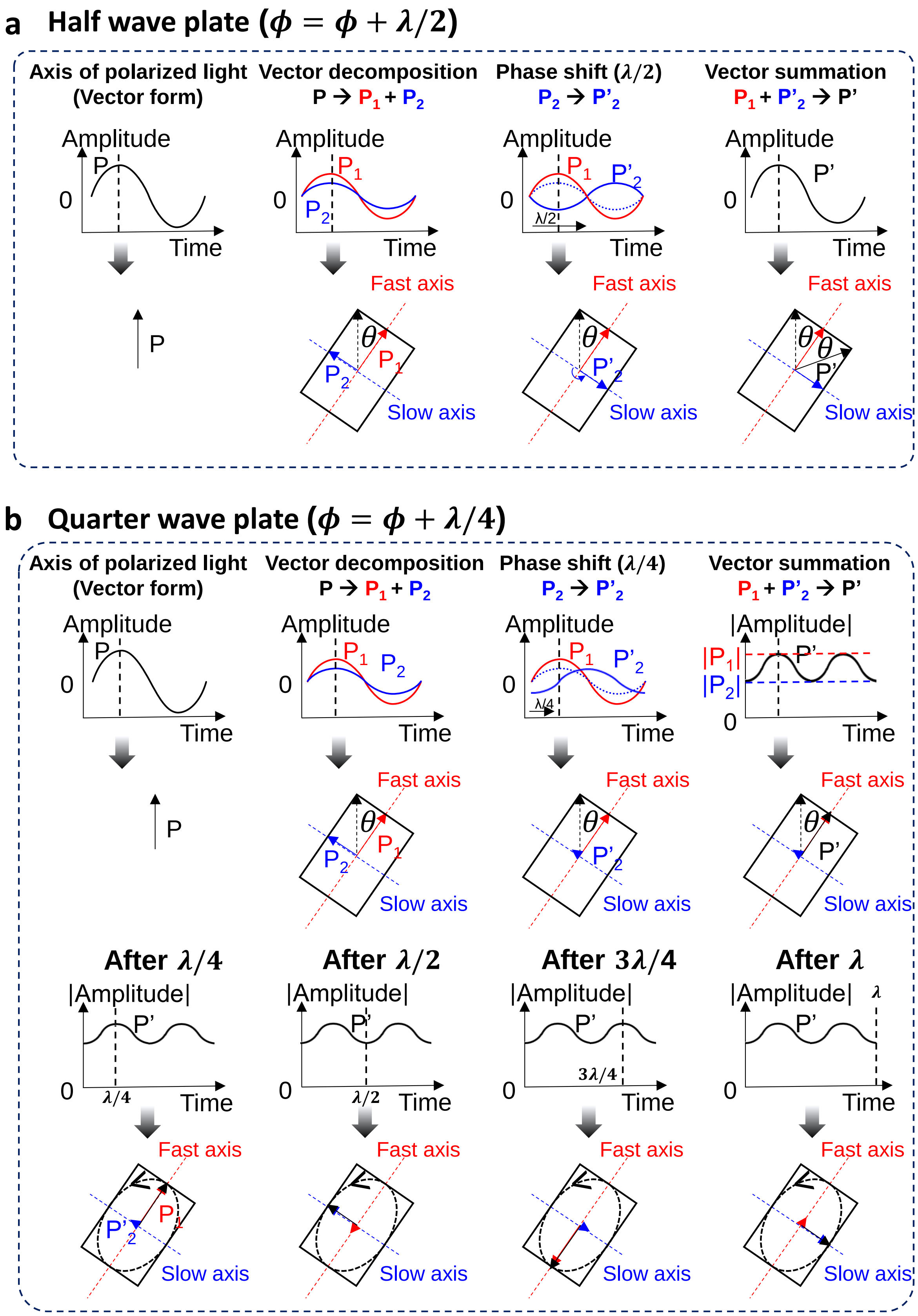

Supplementary Figure 16. Polarization modulation process by **a,** half-wave and **b,** quarter-wave retarders.

A polarized light beam can be initially decomposed into two polarized components aligned along the fast and slow axes of an optical retarder. In the case of a half-wave retarder, the component of light along the slow axis experiences a phase retardation of $\lambda/2$ (= 180°) relative to the component along the fast axis. This phase shift is equivalent to a polarization that is opposite to the original direction. When this light recombines with the component along the fast axis, the overall effect is a rotation of the polarization direction by an angle of 2θ (Supplementary Fig. 16a). For a quarter-wave retarder, the explanation follows a similar principle. This type of retarder introduces a phase difference of $\lambda/4$ (= 90°) between the two components, and when these components recombine, they produce elliptical polarization. Specifically, this results in the creation of circular polarization if the input light was linearly polarized at 45° relative to the retarder axes (Supplementary Fig. 16b).

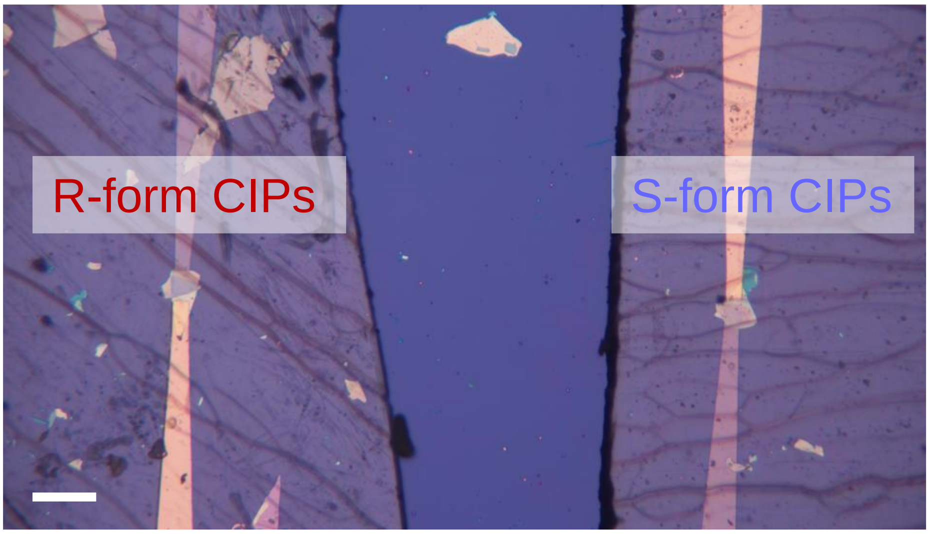

Supplementary Figure 17. Optical microscopy image of zero-dimensional (1×1) polarimetric array of CIPs with a kernel value of +1 (identity) for the R-form CIP and –1 (negation) for the S-form CIP. Scale bar is 50 μm.

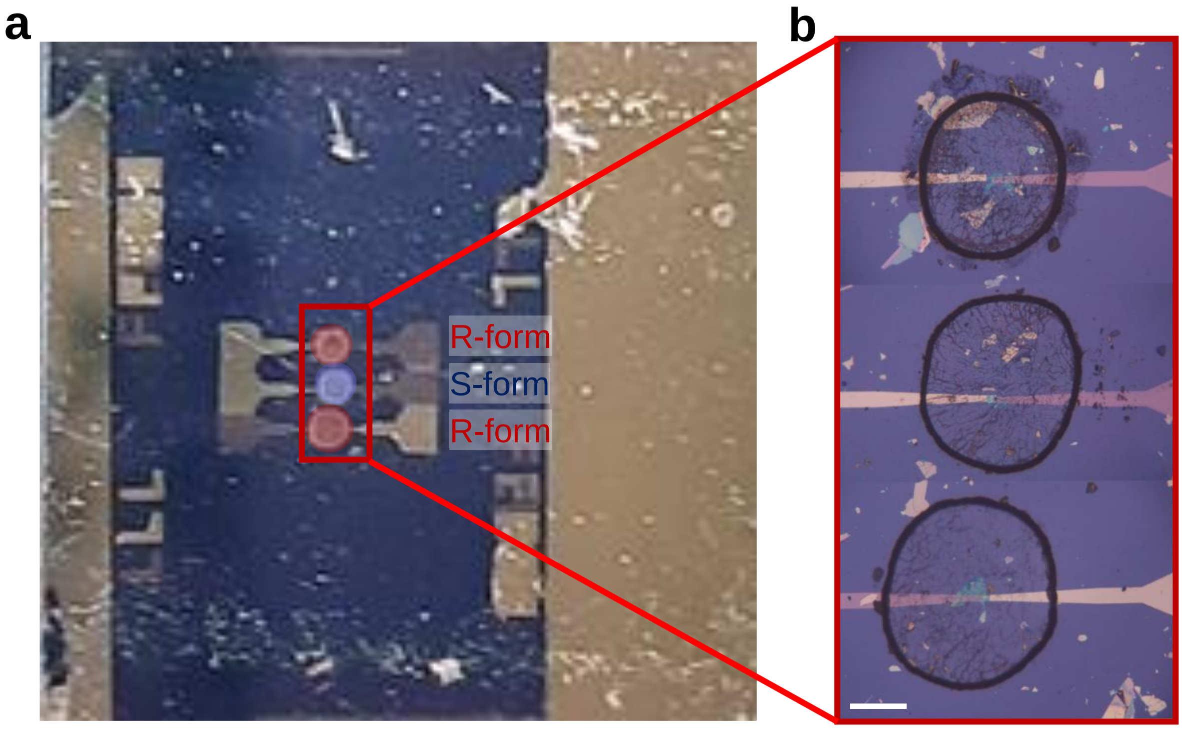

Supplementary Figure 18. a, Photo of 1×3 polarimetric kernel array for mixed identity function and Sobel-x function, and **b,** optical microscopy image. Scale bar is 50 µm.

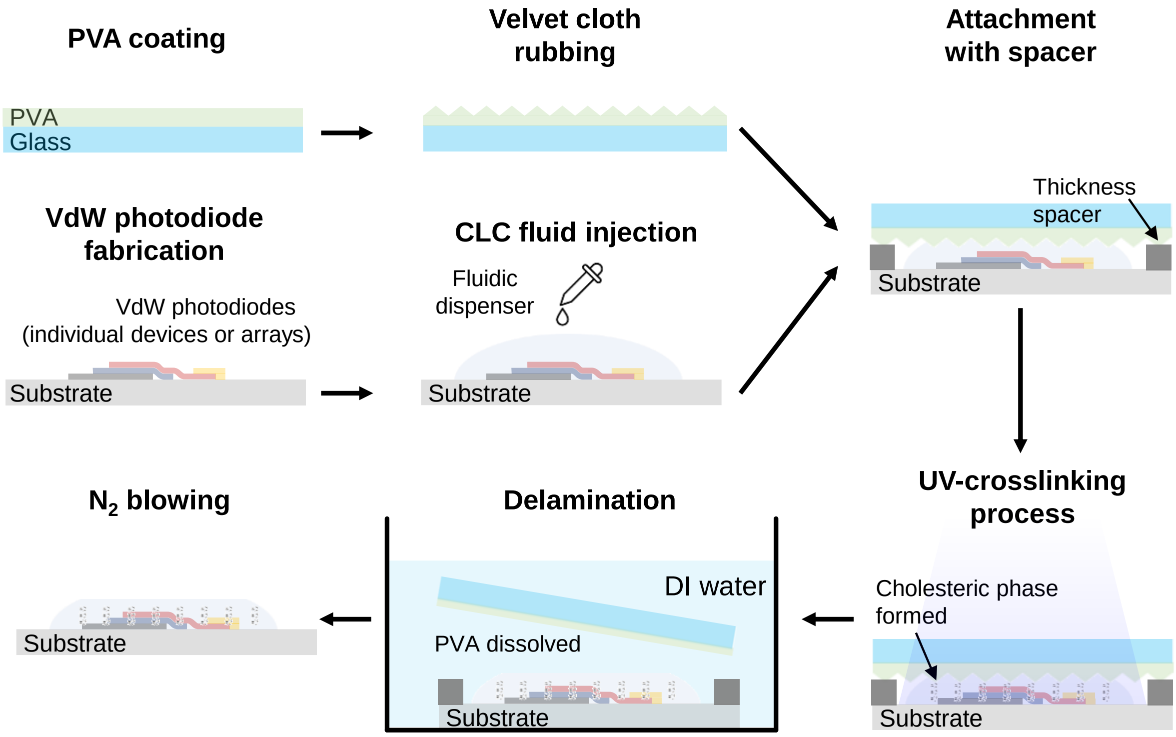

Supplementary Figure 19. Fabrication process of CIPs with direct integration of the localized CLCN.

The CLC liquid was deposited onto a substrate and overlaid with a rubbed PVA-coated glass, with a spacer, to serve as the alignment layer. UV light was then applied to crosslink the CLC dopants, forming an aligned helical structure. The upper glass was subsequently removed by dissolving the PVA layer in DI water. Finally, the device was blown dry with nitrogen gas.

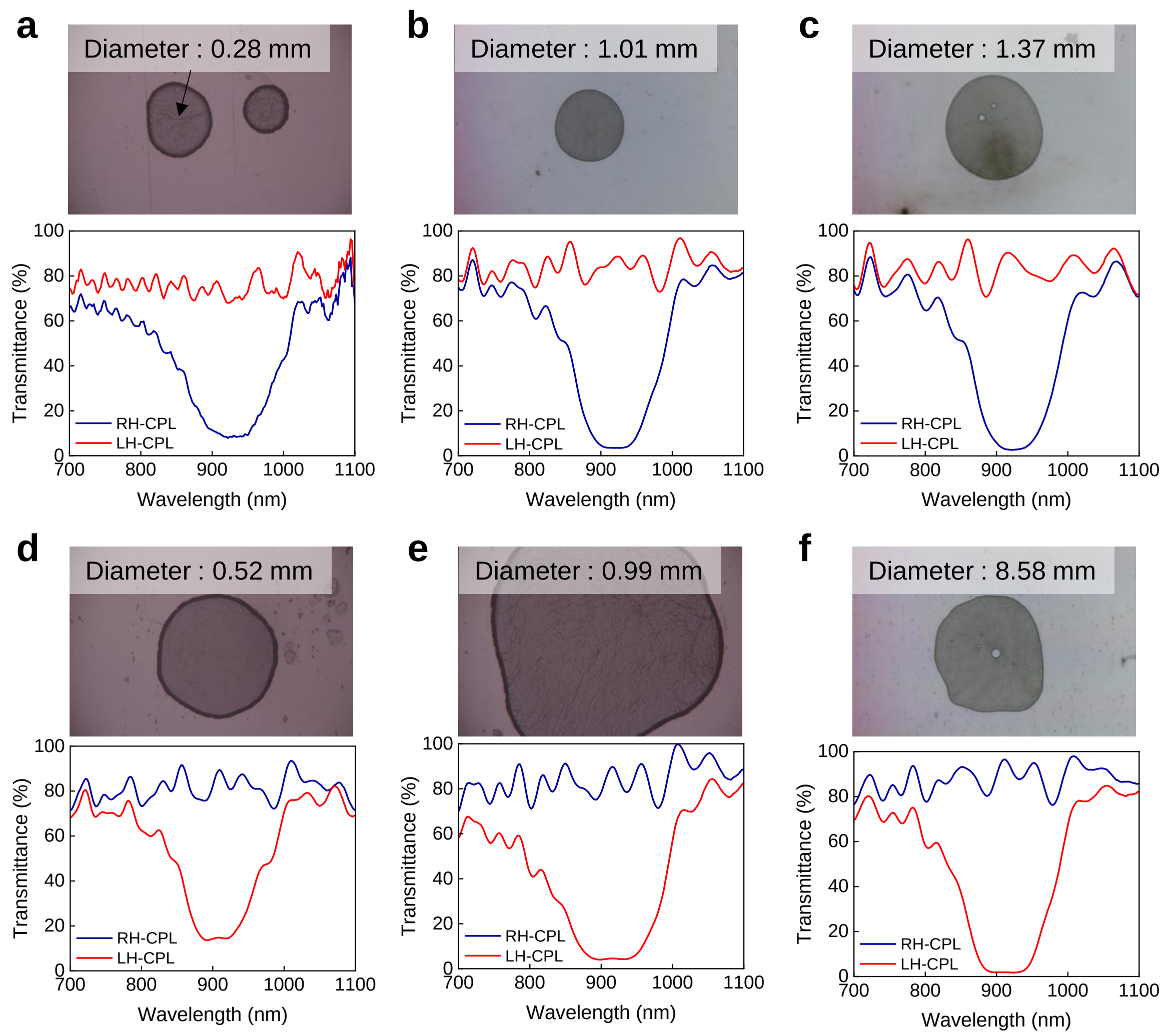

Supplementary Figure 20. Transmittance of localized CLCN. Optical microscopy images and transmittance spectra of localized R-form CLCN with diameters of **a,** 0.28 mm, **b,** 1.01 mm, and **c,** 1.37 mm, and of localized S-form CLCN with diameters of **d,** 0.52 mm, **e,** 0.99 mm, and **f,** 8.58 mm.

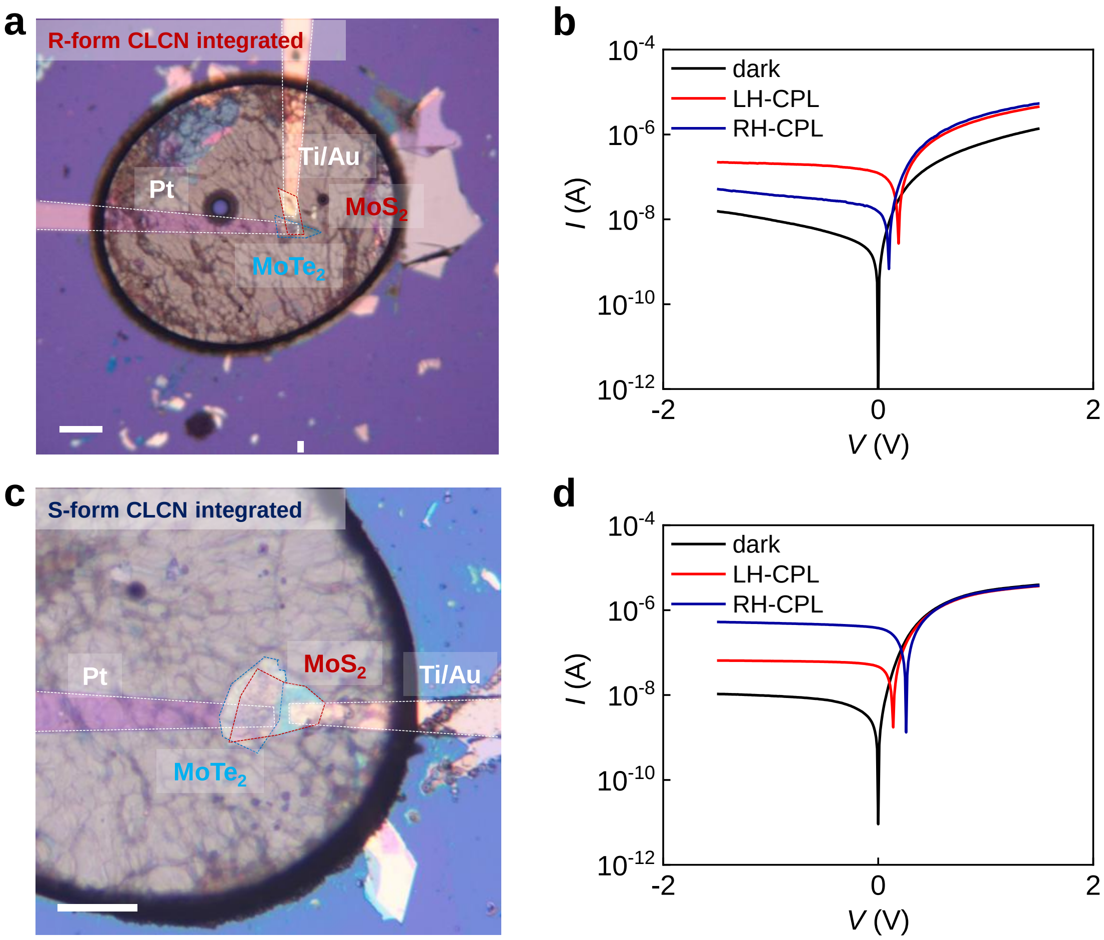

Supplementary Figure 21. *I–V* characteristics of localized CIPs under 904 nm illumination at 100 mW cm^{-2}. Scale bar is 50 µm.

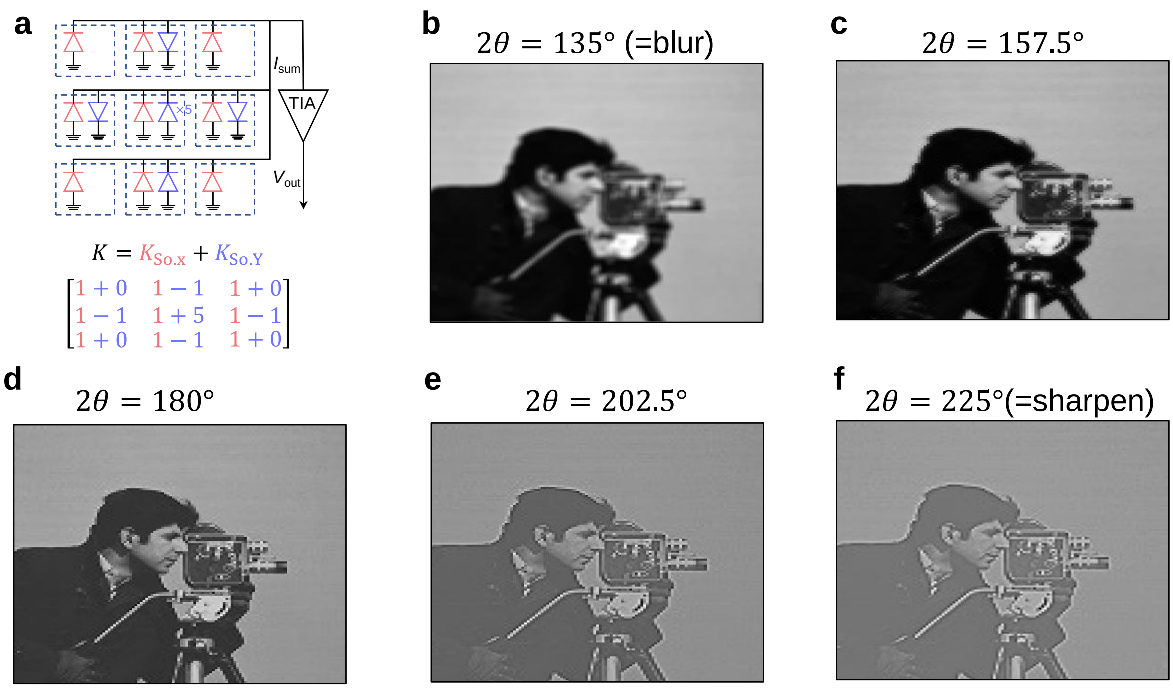

Supplementary Figure 22. Applications of mixed-kernel image processing for blurring and sharpening. **a,** Circuit illustration for deriving output signals from mixed-modality kernels. Processed image for linear polarization angles (2θ) of **b,** 135°, **c,** 157.5°, **d,** 180°, **e,** 202.5°, and **f,** 225°. The Cameraman image is adapted from (© Massachusetts Institute of Technology, used under the CC BY-NC 4.0 license).

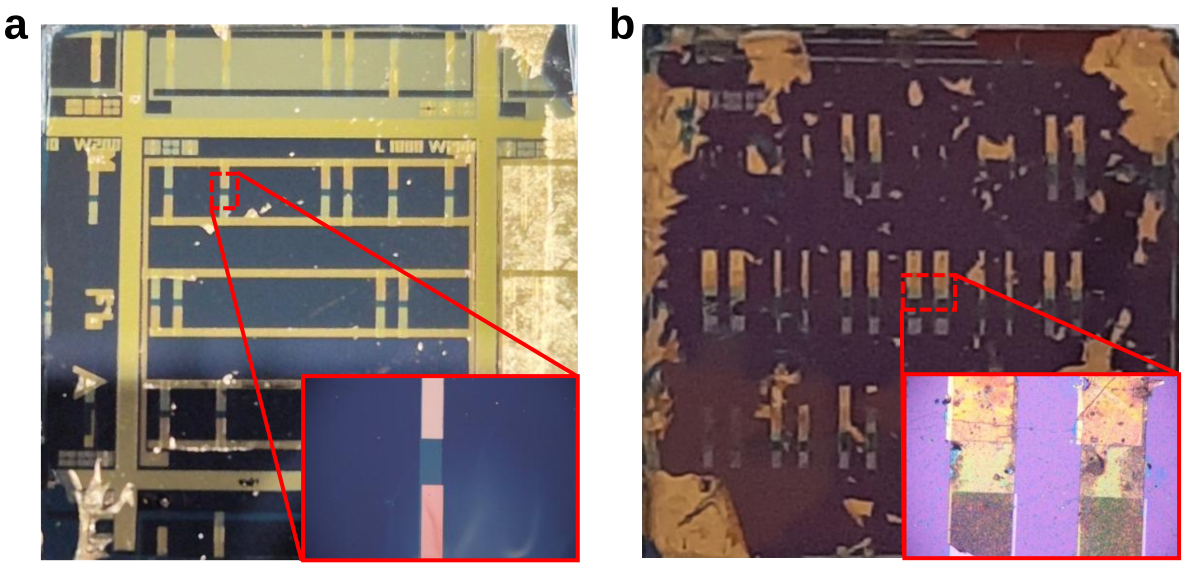

Supplementary Figure 23. Conceptual design of a 3×3 polarimetric kernel array. **a,** Mixed Sobel-X and Sobel-Y polarimetric kernels using CVD-grown MoS_2/WSe_2. **b,** VdW photodiodes via slot-die printing of MoS_2 and WSe_2.

Supplementary Table 1. Comparison of recent in-sensor computing technologies

Reference	S2	S3	S4	S5	S6	S7	S8	This Work
Device architecture	WSe_2	Si	$PdSe_2/MoTe_2$	PDPP3T:PCBM/PVCN/PVA/P3HT:PCBM	Plasma-treated MoS_2	TiO_2/Sb_2Se_3/Si	Gr/Ge	CLCN/$MoTe_2$/ MoS_2
Device functionality	Electrical responsivity control	Electrical responsivity control	Electrical responsivity control	Time-variant responsivity	Gate controlled time-variant responsivity	Chromatic response control	Dynamic kernel Modulation	Polarization dependent responsivity control / chiral-sensitive response
Applications	Pattern recognition	Image processing	Broad-band image processing/ recognition	Photopic adaptation	Scotopic/ photopic adaptation	Classifying spectrally distinctive features	Contrast modulated image processing	Mix-multimodal image processing / chiral decomposition

Supplementary Table 2. Benchmarking table of the optoelectronic properties of circular polarized light detectors. (R) and (S) denote R-form and S-form chiral molecule–based devices, respectively.

Structures	Materials	Wave-length (nm)	Dissymm-etry factor	Responsivity (mA/W)	Detectivity (Jones)	Speed (ms) (Rise/Decay)	Year	Journal	Reference
CP light absorber	(R/S)-PFDTBT, C60, PEDOT:PSS	543	0.007 (R) / −0.017 (S)	-	-	-	2010	Adv. Mater.	S9
CP light absorber	[P(S),M(R)]-Aza[6]H	365	-	0.01	-	2.6	2013	Nat. Photonics	S10
CP light absorber	(R/S)-CPDI-PH NW	460	−0.33 (S)	334	-	-	2017	Adv. Mater.	S11
CP light absorber	(R&S)-α-$(PEA)_2PbI_4$	520	0.274 (R) / −0.228 (S)	-	-	22 / 34	2019	ACS Nano	S12
CP light absorber	(R- and S-α-PEA)PbI_3	365-530	0.02 (R) / −0.02 (S)	464	7.1×10^{11}	1	2019	Nat. Commun.	S13
CP light absorber	(R/S)-ProSQ-C6, PCBM	543	0.08 (R) / −0.10 (S)	-	-	-	2019	Adv. Funct. Mater.	S14
CP light absorber	((R/S)-MBA)$_2PbI_4$, MoS_2	518	0.19 (R) / −0.20 (S)	450	2.2×10^{11}	100	2019	ACS Nano.	S15
CP light absorber	[(R/S)-β-MPA]$_2MAPb_2I_7$	532	0.2 (R)	1100(R)	2.3×10^{11} (R)	1.6 / 2.1 (R)	2020	Angew. Chem. Int. Ed	S16
CP light absorber	(R/S)-ClCPDI-Ph-CF	427-522	0.120 (R) / −0.129 (S)	112900	2.2×10^{16}	50	2020	ACS Nano.	S17
CP light absorber	(R/S)-Ph-C61-BAME	405	1.27 (R) / −0.26 (S)	-	-	~43 / ~43	2020	Adv. Mater.	S18
CP light absorber	[(R&S)-MPA]$_2MAPb_2I_7$, $MAPbI_3$	520	0.67	1.2	1.1×10^{12}	2 / 2.4	2021	ACS Cent. Sci.	S19
CP light absorber	(R/S)-Ortho-π-extended PDI	635	0.057 (R) / −0.054 (S)	450	5.9×10^{9}	-	2021	Nat. Commun.	S20
CP light absorber	[(R/S)-β-MPA]$_4AgBiI_8$	520	0.22 (R)	0.022(R)	$1.2\text{x}10^{7}$(R)	0.58 / 0.96 (R)	2021	Angew. Chem. Int. Ed	S21
CP light absorber	(R,R)/(S,S)-BTP-4Cl, PM6	300-950	0.03 (R) / −0.03 (S)	400	3×10^{11}	~0.05	2022	Small	S22
CP light absorber	(R,R)/(S,S)-BTP-4F, PM6	830	0.01 (R) / −0.015 (S)	0.35	-	0.021	2022	Adv. Mater.	S23
CP light absorber	(R/S)-DPP6T, PC61BM	606	0.17 (R) / −0.16 (S)	280(R) / 150(S)	1.8×10^{11} (R) / 9.91×10^{10} (S)	0.472 / 0.028(R), 0.133 / 0.030(S)	2022	ACS Mater. Lett.	S24
CP light absorber	(R)-AuNP-CsFA-MAPbSn	808	−0.55 (R)	510(S)	2.45×10^{13} (S)	-	2022	Adv. Sci.	S25
CP light absorber	(R/S)-F8T2:aza[6]H, C60, PEDOT:PSS	540	0.85 (R) / −0.85 (S)	-	-	0.007 / 0.007	2022	Adv. Opt. Mater.	S26
CP light absorber	(R/S)-MBOTPA, porphyrin-based TAPP	405	0.00023 (R) / −0.00045 (S)	1000	5.5×10^{8}, 5.25×10^{8}	26.4 / 33.4	2023	Adv. Mater.	S27
CP light absorber	S5011, PCPDTTBTT, PC70BM	300-800	−1.2 (S)	-	2×10^{9}	47.8 / 41.9	2023	Nature	S28
CP light absorber/ Charge transport layer	(R/S)-Ag-based Chiral plasmonic metamaterial, Si	1200-1700	1 (R) / −1 (S)	2	-	-	2015	Nat. Commun.	S29
CP light absorber/ Charge transport layer	(R/S)-Au-based Chiral plasmonic metamaterial, $MoSe_2$	790	0.38 (R) / −0.38 (S)	-	-	100	2020	Nanoscale	S30
CP light absorber/ Charge transport layer	[(R/S)-MBA]$_2CuCl_4$, SWCNT	405	0.25 (R) / 0.194 (S)	452000 (R)		-	2021	ACS Nano	S31
CP light absorber/ Charge transport layer	P(S)-NTPH, 2.6-DPA	556	0.24 (S)	280	-	45 / 46	2022	Nat. Commun.	S32
CP light reflector/ Absorber	(R/S)-CLCN, PODTPPD-BT	750-1000	1.8 (R) / 1.9 (S)	300000	-	260 / 250	2020	Adv. Funct. Mater.	S33
CP light reflector/ Absorber	S-CLCN, PM6, L8BO	530-640	1.62 (S)	400	8.5×10^{14}	1.2 / 7.2	2024	Adv. Mater.	S34
CP light reflector/ Absorber	**(R/S)-CLCN, $MoTe_2$, MoS_2**	**808-904**	**1.88 (R) / −1.90 (S)**	**158 (R) / 102 (S)**	**3.5×10^{8} (R), 1.25×10^{8} (S)**	**0.004 / 0.004**			**This work**

References

1. Xiao, H., Rasul, K., and Vollgraf, R. Fashion-MNIST: a novel image dataset for benchmarking machine learning algorithms. arXiv https://arxiv.org/abs/1708.07747 (2017).

2. Mennel, L. et al. Ultrafast machine vision with 2D material neural network image sensors. *Nature.* **579**, 62-66 (2020).

3. Jang, H. et al. In-sensor optoelectronic computing using electrostatically doped silicon. *Nat. Electron.* **5**, 519–525 (2022).

4. Pi, L. et al. Broadband convolutional processing using band-alignment-tunable heterostructures. *Nat. Electron.* **5**, 248-254 (2022)

5. He, Z. et al. An organic transistor with light intensity-dependent active photoadaptation. *Nat. Electron.* **4**, 522-529 (2021)

6. Liao, F. et al. Bioinspired in-sensor visual adaptation for accurate perception. *Nat. Electron.* **5**, 84-91 (2022)

7. Ouyang, B. et al. Bioinspired in-sensor spectral adaptation for perceiving spectrally distinctive features. *Nat. Electron.* **7**, 705-713 (2024)

8. Yang, Y. et al. In-sensor dynamic computing for intelligent machine vision. *Nat. Electron.* **7**, 225-233 (2024).

9. Gilot, J. et al. Polymer photovoltaic cells sensitive to the circular polarization of light. *Adv. Mater.* **22**, E131–E134 (2010).

10. Yang, Y. et al. Circularly polarized light detection by a chiral organic semiconductor transistor. *Nat. Photonics* **7**, 634–638 (2013).

11. Shang, X. et al. Supramolecular nanostructures of chiral perylene diimides with amplified chirality for high-performance chiroptical sensing. *Adv. Mater.* **29**, 1605828 (2017).

12. Wang, J. et al. Aqueous synthesis of low-dimensional lead halide perovskites for room-temperature circularly polarized light emission and detection. *ACS Nano* **13**, 9473–9481 (2019).

13. Chen, C. et al. Circularly polarized light detection using chiral hybrid perovskite. *Nat. Commun.* **10**, 1927 (2019).

14. Schulz, M. et al. Chiral excitonic organic photodiodes for direct detection of circular polarized light. *Adv. Funct. Mater.* **29**, 1900684 (2019).

15. Ma, J. et al. Chiral 2D perovskites with a high degree of circularly polarized photoluminescence. *ACS Nano* **13**, 3659–3665 (2019).

16. Wang, L. et al. A chiral reduced-dimension perovskite for an efficient flexible circularly polarized light photodetector. *Angew. Chem. Int. Ed.* **59**, 6442–6450 (2020).

17. Shang, X. et al. Surface-doped quasi-2D chiral organic single crystals for chiroptical sensing. *ACS Nano* **14**, 14146–14156 (2020).

18. Shi, W. et al. Fullerene desymmetrization as a means to achieve single-enantiomer electron acceptors with maximized chiroptical responsiveness. *Adv. Mater.* **33**, 2004115 (2021).

19. Zhang, X. et al. Great amplification of circular polarization sensitivity via heterostructure engineering of a chiral two-dimensional hybrid perovskite crystal with a three-dimensional $MAPbI_3$ crystal. *ACS Cent. Sci.* **7**, 1261-1268 (2021).

20. Zhang, L. et al. π-Extended perylene diimide double-heterohelicenes as ambipolar organic semiconductors for broadband circularly polarized light detection. *Nat. Commun.* **12**, 142 (2021).

21. Li, D. et al. Chiral lead-free hybrid perovskites for self-powered circularly polarized light detection. *Angew. Chem. Int. Ed.* **60**, 8415–8418 (2021).

22. Liu, L. et al. Chiral non-fullerene acceptor enriched bulk heterojunctions enable high-performance near-infrared circularly polarized light detection. *Small* **18**, 2202941 (2022).

23. Liu, L., Wei, Z. & Meskers, S. C. J. Semi-transparent, chiral organic photodiodes with incident direction-dependent selectivity for circularly polarized light. *Adv. Mater*. **35**, 2209730 (2023).

24. Liu, L. et al. Building supramolecular chirality in bulk heterojunctions enables amplified dissymmetry current for high-performing circularly polarized light

detection. *ACS Mater. Lett.* **4**, 401–409 (2022).

25. Kim, H. et al. Ultrasensitive near-infrared circularly polarized light detection using 3D perovskite embedded with chiral plasmonic nanoparticles. *Adv. Sci.* **9**, 2104598 (2022).

26. Ward, M. D. et al. Highly selective high-speed circularly polarized photodiodes based on π-conjugated polymers. *Adv. Opt. Mater.* **10**, 2101044 (2021).

27. Gu, Q. et al. Constructing chiral covalent-organic frameworks for circularly polarized light detection. *Adv. Mater.* 2306414 (2023).

28. Song, I. et al. Helical polymers for dissymmetric circularly polarized light imaging. *Nature* **617**, 92–99 (2023).

29. Li, W. et al. Circularly polarized light detection with hot electrons in chiral plasmonic metamaterials. *Nat. Commun.* **6**, 8379 (2015).

30. Jiang, Q. et al. Ultrathin circular polarimeter based on chiral plasmonic metasurface and monolayer $MoSe_2$. *Nanoscale* **12**, 5906–5913 (2020).

31. Hao, J. et al. Direct detection of circularly polarized light using chiral copper chloride–carbon nanotube heterostructures. *ACS Nano* **15**, 7608–7617 (2021).

32. Zhu, D. et al. Organic donor-acceptor heterojunctions for high performance circularly polarized light detection. *Nat. Commun.* **13**, 3454 (2022).

33. Han, H. et al. High-performance circularly polarized light-sensing near-infrared organic phototransistors for optoelectronic cryptographic primitives. *Adv. Funct. Mater.* **30**, 2006236 (2020).

34. Wang, Q. et al. High-performance organic narrow dual-band circular polarized light detection for encrypted communications and color imaging. *Adv. Mater.* **36**, 2312396 (2024).